Journal of Alloys and Compounds 813 (2020) 152136

Contents lists available at ScienceDirect

Journal of Alloys and Compounds

journal homepage: http://www.elsevier.com/locate/jalcom

Unveiling the infrared complex dielectric function of ilmenite $CdTiO_3$

João E.F.S. Rodrigues [a], Mateus M. Ferrer [b], Mario L. Moreira [b], Julio R. Sambrano [c], Renilton C. Costa [d], Ariano D. Rodrigues [e], Paulo S. Pizani [e], Y. Huttel [a], José A. Alonso [a], Carlos Pecharromán [a, *]

[a] Instituto de Ciencia de Materiales de Madrid, Consejo Superior de Investigaciones Cientificas, C/ Sor Juana Inés de la Cruz, 3, 28049, Madrid, Spain
[b] Department of Physics, Federal University of Pelotas, 96160-000, Pelotas, RS, Brazil
[c] Modeling and Molecular Simulations Research Group, São Paulo State University, UNESP, 17033-360, Bauru, SP, Brazil
[d] Department of Environmental Engineering, Federal University of Campina Grande, 58840-000, Pombal, PB, Brazil
[e] Department of Physics, Federal University of São Carlos, 13565-905, São Carlos, SP, Brazil

ARTICLE INFO

Article history:
Received 5 June 2019
Accepted 1 September 2019
Available online 4 September 2019

Keywords:
$CdTiO_3$
Ilmenite
Infrared reflectivity
Effective medium theory
Lattice dynamics
Microwave dielectrics

ABSTRACT

This work presents the infrared active modes of the ilmenite phase of $CdTiO_3$. Since the ilmenite phase of cadmium titanate is unstable in large particle size, the dielectric tensor at the infrared region has been extracted from near normal reflectance of highly reflecting cold pressed powder pellets. The microscopic values of each tensor component were deduced by a new formulation of the effective medium model suitable for anisotropic compacts. This model explicitly takes into account both the matrix and void percolation thresholds, in order to properly determine the dielectric tensor at the region of high frequency longitudinal modes. Both, reflection and absorption experimental data are been confronted with theoretical calculations based on the density functional theory, revealing a great convergence of the values. Additionally, we estimated the quality factor in the microwave region to be: ε_s^x ~27, ε_s^z ~20, and $Q_u \times f$ ~111,000 GHz (at 10 GHz), enabling the ilmenite $CdTiO_3$ material to be employed as central element in circuitry operating at IEEE X-band.

1. Introduction

Cadmium titanate (or $CdTiO_3$) is an *n*-type wide band gap semiconductor oxide with a relatively broad application, including methane [1] and humidity sensing [2], photodegradation of gaseous benzene [3], photoanode for dye-sensitized solar cells [4], and ferroelectricity [5]. From the scientific point of view, this material is an interesting topic for solid state sciences, mainly due to the possibility to be stabilized at room conditions in phases with paramount importance in material sciences as perovskite and ilmenite [6]. In this case, the perovskite is the thermodynamically stable phase, while the ilmenite only can be obtained in submicron powders [7]. Due to the difficulties encountered at growing single-crystals, only few works on its structural and vibrational properties can be found. For instance, Kennedy et al. [7] refined the crystalline structure of $CdTiO_3$ by neutron powder diffraction. Taniguchi et al. [8] exploited the mechanism of ferroelectricity in $CdTiO_3$ by probing the effect of Ca^{2+} substitution. Liebermann provided valuable information on the elasticity property of cadmium titanate [9].

The stabilization of each phase depends on the synthesis conditions. The ilmenite phase, which is known to appear at low temperatures, presents a rhombohedral space group *R*-3 (C_{3i}^2, #148) crystalline structure, being it described by an ordered corundum-type lattice containing stacking layers of edge-sharing CdO_6 and TiO_6 octahedra with 1:1 long-range order. Otherwise, high-temperature conditions lead to the perovskite phase with an orthorhombic space group *Pnma* (D_{2h}^{16}, #62), once cooled down to room temperature. Such a phase undergoes a displacive ferroelectric transition at 80 K to a polar orthorhombic structure with $Pna2_1$ (C_{2v}^9, #33) space group [6]. While the transition from ferroelectric-to-paraelectric phases is reversible, the ilmenite structure becomes perovskite in an irreversible way by sintering or growing a single-crystal.

To the best of our knowledge, there are few comprehensive works reporting infrared spectroscopic data, even less focusing on their complex dielectric function, of $ATiO_3$ ilmenite-type

* Corresponding author.
E-mail address: cpg@icmm.csic.es (C. Pecharromán).
URL: https://www.icmm.csic.es/

https://doi.org/10.1016/j.jallcom.2019.152136
0925-8388/

compounds. It deserves a quote the work of Baran and Boton, which reports the vibrational data of several ilmenites using infrared absorption spectroscopy [10], and Hofmeister who performed the first symmetry assignment of the infrared modes in ilmenites based on the spectroscopic data of fourteen isotopic compounds, including silicates, germanates, titanates, and stannates [11].

With this work, we contribute with a complete description of the infrared active modes in ilmenite $CdTiO_3$ using both infrared specular reflectance and absorption techniques. Such tools have been widely used for single-crystals because it is able to determine the infrared active vibrational modes with a remarkable precision. The infrared reflectance spectroscopy is also recommended to probe the intrinsic microwave loss, since it is mainly dependent on the phonon absorption of anharmonic crystal and polar lattice vibrations [12–15]. However, the method cannot be employed as it for submicron particles because reflectance requires a smooth and large (much larger than the incident wavelength) planar surface. In order to overcome such an issue, we have employed a theoretical and experimental method [16,17], which leads to very satisfactory results for the complex dielectric function derived from the specular reflectance data performed on cold pressed powders. These systems present two problems: it is necessary to obtain a mechanically stable pellet with a flat and very smooth surface, and then it is necessary to determine the dielectric tensor of individual particles from the data of the substance-air composite. Once these problems were conveniently solved, such a procedure has been applied to derive the infrared optical constants of the following isotropic substances: γ-Fe_2O_3 [18], η-Al_2O_3 [19], $Li_{4/3}Ti_{5/3}O_4$ [20].

This procedure has been extended to an uniaxial substance, as it is the tetragonal phase of ZrO_2 [21] or α-Fe_2O_3 [22]. In both cases, the mode assignation was easy, because the IR modes of hematite were previously published [23], and t-ZrO_2 only has two ordinary and one extraordinary modes. However, for an ordinary uniaxial or biaxial substance, many modes should be considered, being very likely that some of them will overlap in several spectral ranges [24,25]. In this sense, a single reflectance spectrum does not supply enough information to determine the spectral position of the transverse and longitudinal phonon frequencies [26]. In this context, the $CdTiO_3$ ilmenite material is a prototype uniaxial dielectric material containing eight infrared active modes ($\Gamma_{IR} = 4A_u \oplus 4E_u$) at Γ-point, and not exhibiting any magnetic property.

Therefore, in this work, we report a new methodology to precisely measure the infrared optical properties (i.e. frequencies of the IR active phonons) of non-isotropic substances which cannot be prepared as single-crystals. For such a purpose, we will need to combine the information from *ab initio* calculations using the density functional theory (DFT) with infrared spectroscopy on powdered samples. DFT gives an approximate position for the modes to be used as a first guess for performing simultaneous non-linear least squares fitting on the reflectance of powder pressed pellets and the absorbance of low concentration composites of the powder in a cesium iodide matrix (IR transparent). As a result, we have been able to provide a univocal and detailed description of the infrared modes in ilmenite $CdTiO_3$. Although this is the first time our methodology has been applied, we think that the results can be extended to other non-isotropic powders.

2. Experimental details

2.1. Synthesis

Conventional solid-state synthesis combined with a high-energy vibratory milling was used to produce fine powders of ilmenite $CdTiO_3$ compound (here after: Il-type $CdTiO_3$), starting from CdO and TiO_2 precursors, as described in a previous published paper [27]. The reactants were mixed for 1 h by milling using deionized water, and then thermally treated in air at 750 °C for 2 h.

2.2. Techniques

A X-ray powder diffraction pattern was recorded at room temperature in a Bruker D8 Advance, with Cu-K_α radiation (40 *k*V and 30 *m*A, λ = 1.54053 Å) and *LynxEye* rapid detector, over a 2θ interval from 15° to 85° with step size of 0.02° and step time of 6 s. A Le Bail fitting was conducted using the *FullProf* program [28] in order to determine the lattice parameters. Morphological features were characterized by an *Inspect* F-50 scanning electron microscope (SEM, FEI Netherlands), operating at 5 *k*V.

For the XPS measurements, the powder samples were deposited on clean double-stick carbon tape, loaded in a vacuum load-lock chamber, and then transferred in the ultra-high vacuum XPS system. The XPS chamber has a base pressure of 10^{-10} mbar and is equipped with a hemispherical electron energy Analyzer (*SPECS* Phoibos 100 spectrometer) and an Al K_α (1486.29 eV) X-ray source. The angle between the hemispherical analyzer and the plane of the surface was kept at 60°. Wide scan spectrum (or survey) was recorded using an energy step of 0.5 eV and a pass-energy of 40 eV, while specific core levels spectra (Cd 3*d*, Ti 2*p*, O 1*s*, and C 1*s*) were acquired using an energy step of 0.1 eV and a pass-energy of 20 eV. Data processing was performed with *CasaXPS* software. The absolute binding energies of the photoelectron spectra were determined by referencing to the C 1*s* core level at 285 eV [29]. The contributions of the Al K_α satellite lines were subtracted.

The infrared reflectivity spectra were recorded in a Bruker IFS 66V Fourier-transform spectrometer, equipped with a specular reflectance cell and a fixed incident angle of 12°. For the measurements, powder samples were cold pressed into pellets in vacuum condition under ~800 MPa using a YTZP (yttria-tetragonal-partially-stabilized-zirconia) pressing die with a optically smooth surface in order to produce pellets with high-quality reflecting surfaces. The degree of compaction was $f = 0.56$, slightly inferior to the so-called Random Close Packing volume concentration ($f_{RCP} \sim 0.64$), which is the most common packing efficiency of non-ordered spheres.

3. Computational details

Quantum simulations were performed according to the density functional theory (DFT) using *B3LYP* hybrid functional implemented on *CRYSTAL*17 package [30,31]. The cadmium, titanium, and oxygen atomic centers were defined by POB_TZVP [32], 8–6411(31d)G [33], and 8–411(1d)G [33] all-electron basis sets, respectively. The calculations were conducted with the truncation criteria for the Coulomb and exchange series controlled by a set of five thresholds (10^{-8}, 10^{-8}, 10^{-8}, 10^{-8}, and 10^{-16}), and shirking factors set of 8 and 8 for Pack-Monkhorst and Gilat net, respectively. Structural data for the input file were extracted from the ICSD Card #262708. Infrared phonons were determined from numerical second derivatives of the total energy, while dielectric constant and mode intensities were performed with a perturbative treatment in presence of an electric field perturbation according to the Coupled Perturbed Hartree-Fock/Kohn-Sham method (CPHF/KS) [34,35].

4. Experimental results: characterization

Fig. 1a summarizes the X-ray powder diffraction pattern of Il-type $CdTiO_3$ and its Le Bail refinement. The fitting confirmed the occurrence of the rhombohedral space group *R*-3 for the $CdTiO_3$ phase. A careful analysis of the pattern revealed signals of cadmium

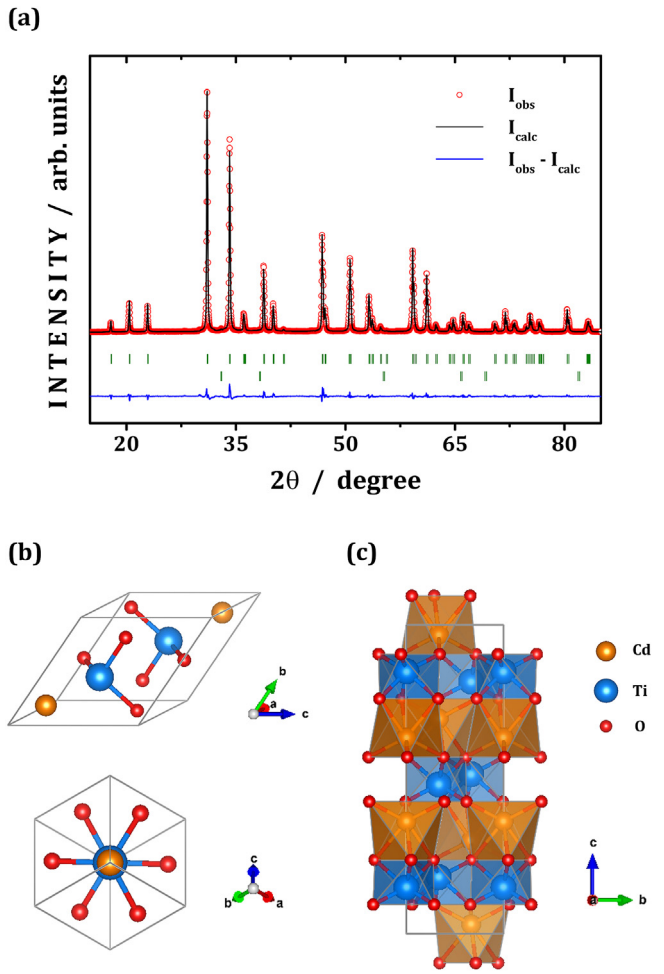

Fig. 1. (a) Le Bail refinement results for ll-type $CdTiO_3$. Red open circles are assigned to experimental data, black line refers to calculated profile, blue line is the difference pattern between experimental and calculated data, and dark green bars denote the Bragg reflections. (b) 3D and $[111]_R$ views of the *R*-3 structure in its rhombohedral description. (c) $[100]_R$ view of the *R*-3 unit cell at its hexagonal representation. (For interpretation of the references to colour in this figure legend, the reader is referred to the Web version of this article.)

oxide as a secondary phase (<2%) in view of the small peak at $2\theta \sim 32.9°$. The lattice parameters of the rhombohedral unit cell were estimated, as follows: $a_R = 5.8075(2)$ Å and $\alpha_R = 53.72(2)°$. Fig. 1b shows a schematic representation of the rhombohedral $CdTiO_3$ with two molecules per unit cell ($Z = 2$). From such a structure, the 1:1 ordered motif layers of CdO_6 and TiO_6 octahedra alternate along the $[111]_R$ direction, see in Fig. 1c.

Fig. 2a shows the relative frequency distribution of the particle diameter and the lognormal fitting for the as-prepared $CdTiO_3$ powders. The representative micrograph in Fig. 2b with microstructural features was evaluated by scanning electron microscopy. A statistical counting using the Feret diameter definition revealed the mean particle diameter (D_c) of 118 nm with a standard deviation (σ) of 0.3 nm, as derived from the lognormal fitting of the statistical distribution. In this counting, a total of 436 particles were considered. The diameter, however, may vary between 40 and 280 nm. The average ratio $\langle r \rangle$ between the principal axes of the spheroidal objects was also estimated: $\langle r \rangle \sim 1$, which means that the particle resembles more closely the spherical shape. The achievement of almost nanosized particles is a consequence of the high-energy ball milling for powder synthesis, as recently shown elsewhere [36].

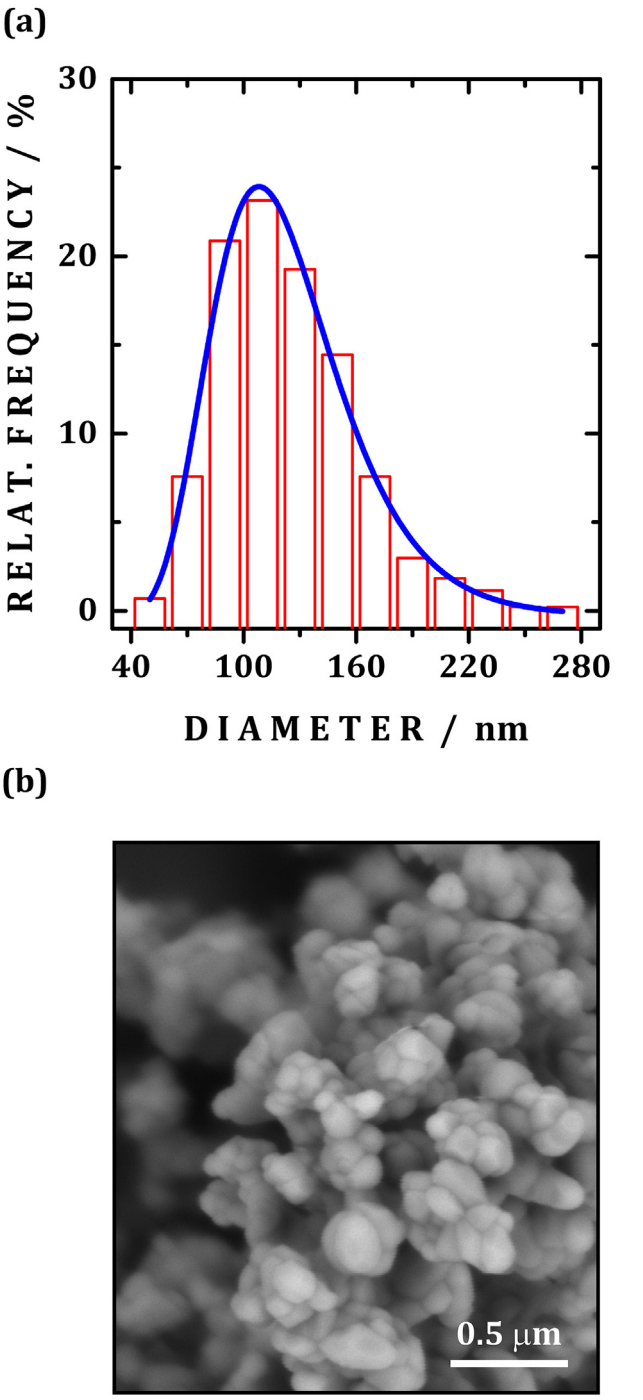

Fig. 2. Particle diameter distribution (a) of ll-type $CdTiO_3$ as-prepared powders shown in SEM micrograph (b). The blue line represents the lognormal fitting performed in the statistical counting, which revealed a mean particle diameter (D_c) of 118 nm with standard deviation (σ) of 0.3 nm. (For interpretation of the references to colour in this figure legend, the reader is referred to the Web version of this article.)

XPS analysis was employed to probe the surface chemistry and the oxidation states of the Cd and Ti centers. Fig. 3a exhibits the survey spectrum of ll-type $CdTiO_3$ powders, in which Cd, Ti, and O elements clearly appeared. Fig. 3b displays the high resolution photoelectron spectrum at Cd 3*d* core energy. The fitting process by a Shirley background model revealed four components ascribed to the Cd^{2+} cations of CdO and $CdTiO_3$. Two photoelectron peaks at binding energies of 405.4 and 412.3 eV represent the spin-orbit

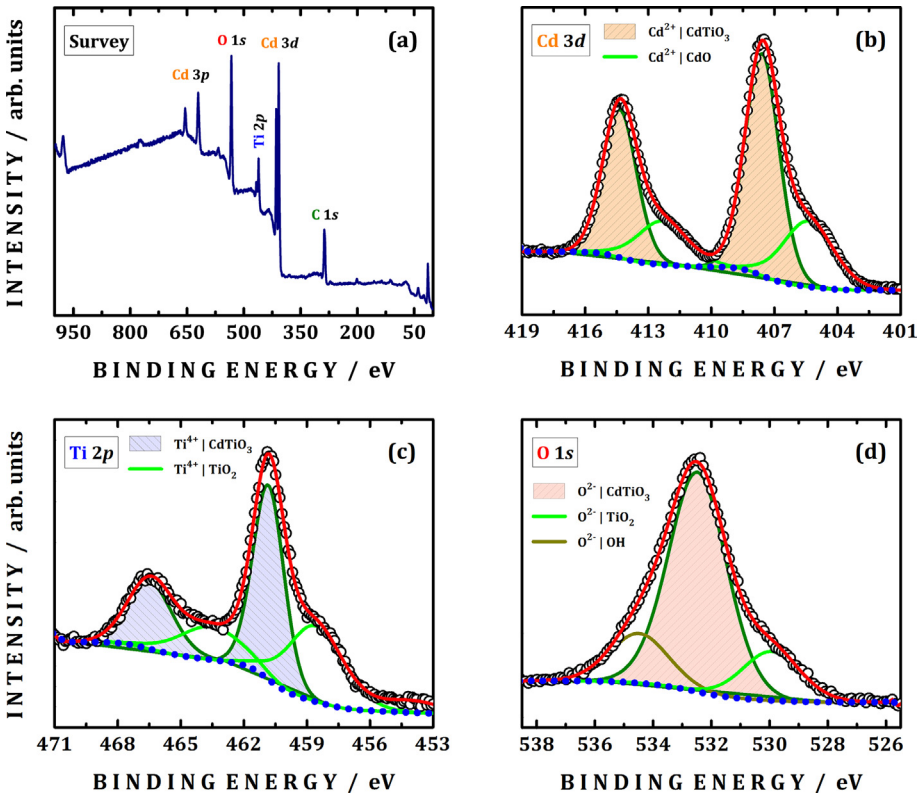

Fig. 3. Photoelectron spectra of the Il-type $CdTiO_3$ powders. (a) Survey scan, (b) Cd 3*d*, (c) Ti 2*p*, and (d) O 1*s*. Open circles and red lines denote the experimental and fitted data, respectively. Green lines represent the components employed during the fitting process and dotted blue lines the Shirley-type background function. (For interpretation of the references to colour in this figure legend, the reader is referred to the Web version of this article.)

separation of the Cd 3*d* spectrum into Cd $3d_{5/2}$ and Cd $5d_{3/2}$ photoemissions [37], respectively. Such a splitting of ~6.9 eV is due to the Cd^{2+} of CdO precipitated after the synthesis process [38]. The other two photoelectron peaks at 407.6 and 414.3 eV are ascribed to the spin-orbit splitting, with ΔE ~6.7 eV, of Cd^{2+} from $CdTiO_3$ compound [39].

The Ti 2*p* photoelectron spectrum of $CdTiO_3$ sample is shown in Fig. 3c. Here, a complex structure can be noticed with four components, as revealed by the fitting process. The most intense photoelectron peak at 460.8 eV and its splitted counterpart at 466.4 eV may be attributed to the Ti^{4+} from $CdTiO_3$ with a spin-orbit split of ~5.6 eV. Two shoulder peaks at binding energies of 458.6 and 463.5 eV correspond to the spin-orbit splitting of the Ti 2*p* spectrum into Ti $2p_{3/2}$ and Ti $2p_{1/2}$ photoemissions [40,41], respectively, being attributed to the Ti^{4+} of TiO_2. However, titanium oxide phase was not detected in XRD pattern in Fig. 1a, which suggests that such a phase is only deposited on the particle surfaces.

High resolution O 1*s* photoelectron spectrum in Fig. 3d was decomposed into an intense peak at 532.5 eV and two shoulder peaks at binding energies of 534.5 and 529.9 eV. The lowest energy peak is attributed to oxygen anions bound to Ti cations in the TiO_2 lattice [42,43]. The main peak denotes the oxygen anions from the $CdTiO_3$ lattice. The photoelectron peak centered at 534.5 eV may be attributed to adsorbed OH species [44,45]. Since the photoelectron emission from the oxygen anions in cadmium titanate accounts for 69% in percentage area, it is expected that these satellite effects should not play a role for the dielectric loss in microwave regime.

The Brillouin zone-center vibrational modes of Il-type $CdTiO_3$ were determined in our earlier work [27]. As a matter of completeness, the mode distribution will be briefly summarized using the irreducible representation of the C_{3i} factor-group [46]. As observed in Fig. 1b, cadmium and titanium atoms lie at the 3-fold axis (C_3) with two equivalent positions for each one, while oxygen anions locate at 1-fold axis (C_1) with six equivalent positions. The summation of the site contribution leads to 10 Raman ($\Gamma_R = 5A_g \oplus 5E_g$) and 8 infrared ($\Gamma_{IR} = 4A_u \oplus 4E_u$) active modes. The complete description of the Raman modes in Il-type $CdTiO_3$ can be found in Ref. [27]. Then, at room condition, one may expect four bands in the infrared spectrum of this material for each polarization A_u and E_u. Before our discussion on the infrared modes, the theoretical aspects behind the spectroscopic data analysis will be briefly exposed.

5. Effective medium theory for powder pellets with variable percolation thresholds

Because the ilmenite phase of $CdTiO_3$ is unstable for particle size larger than a micron, it is impossible to fabricate single-crystals to measure the optical properties along the A_u and E_u polarizations following the standard methodology. However, powder compacts of optically isotropic substances have been successfully analyzed by measuring the specular reflection of pressed powder pellets and by using an effective medium approximation to calculate the dielectric constant of the system composed by powder and air. One can expect that the effective properties follow the rules of mixtures of reflectance, or even in refractive index or permittivity. Nevertheless, this rule can be only applied when grain dimensions are larger than the incident wavelength [47], while for permittivity, the corresponding rule of mixtures only works for composites made by small particles with low contrast between the refractive indices of matrix and inclusions. In the latter case, percolation-based models [48–50] better approaches to the microscopic electromagnetic field distribution. In fact, when the dielectric constant of one of the

phases is much larger than the other, which customary happens at IR frequencies close to the transverse and longitudinal modes (*TO*, *LO*), the effective properties of the composite abruptly varies.

Although mathematical deductions state a percolation threshold is as low as $f = 0.16$ for 3D random systems, real systems always display some degree of ordering, so that the experimental percolation threshold strongly depends on the microstructure [51–57]. In that sense, any realistic model of effective dielectric constant should contain this parameter as an input variable. Therefore, one of us developed an effective medium approach, which is suitable for isotropic or anisotropic substances, that allows inputting the refractive index as a variable [16,17,58,59]. Using this approach, the optical phonons of a large set of substances could be accurately analyzed [16,18–21,58,60].

As a first approach, we tried to employ the same method on this substance. However, Il-type $CdTiO_3$ IR vibrational properties are more challenging, because it is an anisotropic system with four modes for each polarization ($4A_u \oplus 4E_u$). When we used the previously published models, we should first speculate the assignation of each IR reflectance band, and all of our tries resulted in a non-satisfactory fitting for larger wavenumbers. Specifically, in this substance, a weak A_u mode appears very close to the longitudinal frequencies of both A_u and E_u modes, where standard percolation model does not apply. In this spectral region, the strong modes drive the dielectric constant to values below 1, so that it is smaller than that of the air. Consequently, the percolation criterion should be applied to the air instead to particles, because only when voids become connected, and the effective dielectric constant will substantially modify. In other words, if ε_p, ε_m, and $\langle\varepsilon\rangle$ are the dielectric constants of inclusions, matrix, and effective medium, respectively, we need to consider two critical concentrations of particles, f_p and f_m, at which the effective dielectric constant abruptly change its value. Indeed, in all the effective and spectral representation models [49], two percolation thresholds, both for inclusions and matrix phases can also be established. This duality represents the possibility of describing the composite as a function of parameters of particles or matrix. Analytically, the percolation threshold for particles is given by introducing the assumption $\varepsilon_p \gg \langle\varepsilon\rangle \gg \varepsilon_m$ into the effective dielectric model, while the matrix critical concentration, f_m is determined by the approximation $\varepsilon_p \ll \langle\varepsilon\rangle \ll \varepsilon_m$.

Among effective models which include two variable percolation thresholds, only the effective medium theory allows us to include anisotropic particles. Indeed, spectral representation formalism may be the natural choice, because is the one that includes the more precise geometrical information of the composite and introduces both percolation thresholds in a simplest way, but unfortunately, up to date, it only has been developed for binary mixtures of isotropic materials. In this way, we have modified one effective medium approximation suitable for anisotropic materials, introduced in Refs. [17,59], to be able for including percolation thresholds of both phases as well as the shape of particles.

When we use an effective medium approximation for a powder compact, truly, we are considering a binary medium (particles and air) with different ellipsoidal shapes and orientations. According to Refs. [17,59], we only pay attention to the shape of voids, which determine the percolation factor of particles. However, if we also consider a possible preferential orientation of voids it is possible to define both the percolation factor for particle and voids. The most general effective medium theory (EMT) formula [59] can be written as:

$$\langle\varepsilon\rangle = \frac{(1-f)\sum_j \frac{c_{mj}\varepsilon_{mj}}{(1-L_{mj})\langle\varepsilon\rangle + L_{mj}\varepsilon_{mj}} + f\sum_j \frac{c_{pj}\varepsilon_{pj}}{(1-L_{pj})\langle\varepsilon\rangle + L_{pj}\varepsilon_{pj}}}{(1-f)\sum_j \frac{c_{mj}}{(1-L_{mj})\langle\varepsilon\rangle + L_{mj}\varepsilon_{mj}} + f\sum_j \frac{c_{pj}}{(1-L_{pj})\langle\varepsilon\rangle + L_{pj}\varepsilon_{pj}}}. \quad (1)$$

In this equation, ε_{mj} and ε_{pj} are the diagonal components of the dielectric tensor of the matrix and particles, f the volume concentration of phase p, L_{mj} and L_{pj} their corresponding depolarization factors along the j axis, and c_{mj} and c_{pj} the average of the projection of the unit vector parallel to the optic axis onto the applied electric field. In the case of powder pressed pellets, the matrix (i.e. air) is isotropic, so that the dielectric tensor has all the components identical: $\varepsilon_{mj} = \varepsilon_m$. Additionally, for sake of simplicity, we only will consider randomly oriented particles. This constriction ($c_{pj} = {}^1/_3$) ensure us that the composite is optically isotropic. With these simplifications, Eq (1) can be written as follows:

$$(1-f)\left[\frac{2c_{mx}(\langle\varepsilon\rangle - \varepsilon_m)}{(1-L_{mx})\langle\varepsilon\rangle + L_{mx}\varepsilon_m} + \frac{c_{mz}(\langle\varepsilon\rangle - \varepsilon_m)}{(1-L_{mz})\langle\varepsilon\rangle + L_{mz}\varepsilon_m}\right] + \frac{f}{3}\left[\frac{2(\langle\varepsilon\rangle - \varepsilon_{px})}{(1-L_{px})\langle\varepsilon\rangle + L_{px}\varepsilon_{px}} + \frac{(\langle\varepsilon\rangle - \varepsilon_{pz})}{(1-L_{pz})\langle\varepsilon\rangle + L_{pz}\varepsilon_{pz}}\right] = 0. \quad (2)$$

where, the geometric parameter satisfies the following relationships [59]:

$$\begin{cases} 2L_{mx} + L_{mz} = 1 \\ 2L_{px} + L_{pz} = 1 \\ 2c_{mx} + c_{mz} = 1 \end{cases}. \quad (3)$$

In this form, it is easy to estimate the percolation thresholds of this equation. Thus, the percolation for particles f_p is the volume concentration, which satisfies $\varepsilon_p \gg \langle\varepsilon\rangle \gg \varepsilon_m$, i.e.

$$\left(1-f_p\right)\left[\frac{2(1-c_{mz})}{1+L_{mx}} + \frac{c_{mz}}{1-L_{mz}}\right] - \frac{f_p}{3}\left[\frac{4}{1+L_{pz}} + \frac{1}{L_{pz}}\right] = 0 \quad (4)$$

and then

$$f_p = \frac{\frac{2(1-c_{mz})}{1+L_{mx}} + \frac{c_{mz}}{1-L_{mz}}}{\frac{2(1-c_{mz})}{1+L_{mx}} + \frac{c_{mz}}{1-L_{mz}} + \frac{4/3}{1+L_{pz}} + \frac{1/3}{L_{pz}}}. \quad (5)$$

Similarly, the percolation threshold referring to the matrix phase is given for the condition $\varepsilon_p \ll \langle\varepsilon\rangle \ll \varepsilon_m$, i.e.

$$\frac{f_m}{3}\left[\frac{4}{1+L_{pz}} + \frac{1}{1-L_{pz}}\right] - (1-f_m)\left[\frac{2(1-c_{mz})}{1+L_{mz}} + \frac{c_{mz}}{L_{mz}}\right] = 0 \quad (6)$$

and then

$$f_m = \frac{\frac{2(1-c_{mz})}{1+L_{mz}} + \frac{c_{mz}}{L_{mz}}}{\frac{2(1-c_{mz})}{1+L_{mz}} + \frac{c_{mz}}{L_{mz}} + \frac{4/3}{1+L_{pz}} + \frac{1/3}{1-L_{pz}}}. \quad (7)$$

While L_{pz} is experimentally determined by the aspect ratio of the particles, the parameters L_{mz} and c_{mz} have not any constriction, so that, by using equations (5) and (7), they can be established in such manner that the percolation thresholds, f_p and f_m, take the desired values. According to some previous studies in such pellets,

the percolation threshold of particles seem be similar to the volume concentration, typically from 0 to 10% below the nominal concentration [16], while voids percolation threshold seems to be very close to 1, which means that the matrix connectivity is very rich [61]. We can use these set of values, for f_p and f_m, as a first approximation, to introduce these parameters into Eq (3) for the non-linear least square fitting to experimental results. For the mathematical implementation, we have written a *MATLAB®* code which takes into account the expansion of Eq (2) as a form of a fourth degree polynomial in $\langle\varepsilon\rangle$ being the coefficients algebraic expression containing L_m and c_m which have been previously determined by Eqs (5) and (7) from f_p and f_m.

In order to visualize the effect of the percolation threshold of matrix into the effective properties of the composite, we have hypothesized an isotropic solid with a strong phonon, with transverse and longitudinal frequencies at 400 (ω_{T1}) and 900 cm^{-1} (ω_{L1}) with a weak mode at 700 cm^{-1} (ω_{T2}), which is very similar to the MgO infrared phonon distribution [62]. The filling fraction has been fixed to $f = 0.56$ and the particle percolation threshold as $f_p = 0.50$. In case of non-oriented matrix voids ($c_{mz} = 1/3$), its percolation threshold is $f_m = 0.86$. In Fig. 4, we have done calculations following the generalized model for $f_m = 0.60–1$. It can be seen that the spectral region around the transverse mode (400 cm^{-1}) remains almost unchanged, while for wavenumbers close to the longitudinal mode (500–850 cm^{-1}), the reflectance and the dielectric constant strongly depends on f_m. Indeed, the high frequency part of reflectance spectra has been always the more problematic to fit, because this region has dielectric constant with very small values, so that any error in vibrational parameters has a strong effect in this part of the reflectance signal in a manner that it can be very visible or disappear in the reflectance spectrum. Therefore, we have found that introducing a variable percolation

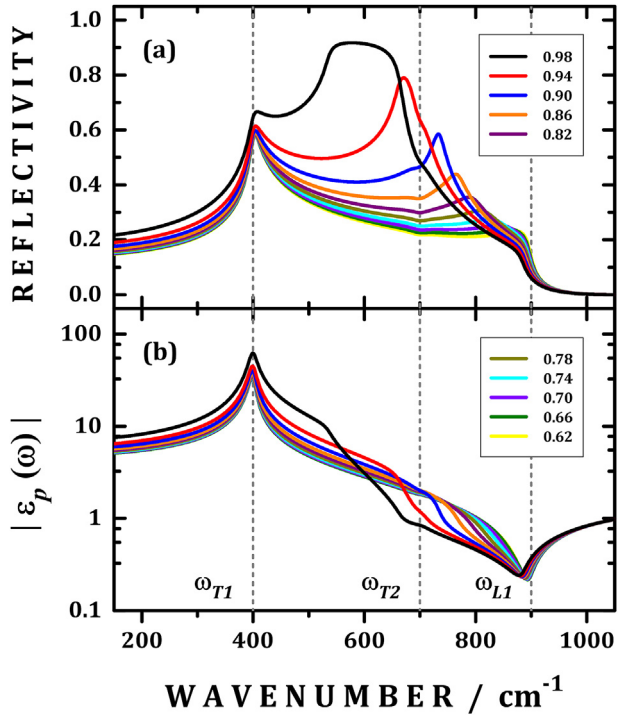

Fig. 4. Infrared reflectivity (a) and absolute permittivity (b) spectra of a hypothetic isotropic solid containing a strong phonon with transverse and longitudinal frequencies at 400 (ω_{T1}) and 900 (ω_{L1}) cm^{-1}, besides a weak band at 700 cm^{-1} (ω_{T2}). Each curve was calculated for different percolation threshold (f_m) values ranging from 0.6 up to 1.

for matrix, the goodness of fitting improves remarkably.

Another problem we have found in anisotropic solids is that, frequently, modes of different optical axis have a similar frequency. This fact makes very difficult to distinguish the contribution of those modes by using only a single spectrum [25]. In order to eliminate that ambiguity, we have considered to perform a simultaneous fitting of reflectance data from a dense powder compact as well as absorbance measurements of dilute dispersion of the same powder into an infrared halide transparent matrix (CsI, in this case). In both cases, we deal with composites, but while for pressed pellets, the particles are percolated, in the case of halide matrix samples, the particles remain isolated. Also for both cases, the polariton resonance of composites, i.e. Fröhlich modes [63], appear between the transverse and longitudinal modes. However, for percolated systems, the Fröhlich modes are very close to the transverse frequency, while for diluted system of spherical particles it appears between transverse and longitudinal bands, more specifically at the so-called Fröhlich frequency, which as a first approximation can be written as: $\omega_F = \omega_T + 1/3(\omega_L - \omega_T)$. This shift is enough to distinguish from modes with similar transverse frequencies in different optical axis, since the splitting (ω_L–ω_T) differs for each polarization.

In order to determine the phonon frequencies, on the one hand, we used the near normal reflectance, which through the Fresnel relation allows determining the effective dielectric constant of the pressed pellet $\langle\varepsilon\rangle_R$:

$$R_{th} = \left|\frac{\sqrt{\langle\varepsilon\rangle_R} - 1}{\sqrt{\langle\varepsilon\rangle_R} + 1}\right|^2. \tag{8}$$

On the other hand, the absorbance has been modelled through the findings described elsewhere [51]. According to such a study, particles tends to agglomerate when halide crystals grow during pressure sintering, so that the observed filling fraction may be several orders of magnitude larger than the nominal one. In this respect, we have left the effective concentration as a fitting parameter, as well as the effective thickness of the sample. The experimental absorption is given by:

$$A_{\exp} = \frac{4\pi}{\log(10)}\omega \mathrm{Im}(\sqrt{\langle\varepsilon\rangle_A})d_{eff}, \tag{9}$$

where, ω is the wavenumber, d_{eff} is the effective thickness, and $\langle\varepsilon\rangle_A$ the effective dielectric constant of the diluted suspension calculated using Eq (2) with the corresponding parameters of f_{eff}, f_p, and f_m. The goodness of the fit ($\Re$) was defined as follows:

$$\Re^2 = \frac{\sum\left(|R_{\exp} - R_{th}|^2 + |A_{\exp} - A_{th}|^2\right)}{\sum\left(R_{\exp}^2 + A_{\exp}^2\right)}. \tag{10}$$

Although $\langle\varepsilon\rangle_R$ and $\langle\varepsilon\rangle_A$ take different values, both have been calculated using Eq (2). Additionally, for each effective dielectric constant, two sets of percolation thresholds have been introduced as fitting parameters. The description of each component, A_u and E_u, of the dielectric tensor of the particles was performed using the model introduced by Gervais and Piriou (also known as four-parameter semi-quantum model or FPSQ), who factorized the complex dielectric function [13], as follows:

$$\varepsilon_p(\omega) = \varepsilon_\infty \prod_{k=1}^{N} \frac{\omega_{kL}^2 - \omega^2 + i\omega\gamma_{kL}}{\omega_{kT}^2 - \omega^2 + i\omega\gamma_{kT}}, \tag{11}$$

such that, ω_{kT} and ω_{kL} denote the frequencies of the transverse (T) and longitudinal (L) optical branches of the k-th phonon,

respectively, and γ_{kT} and γ_{kL} the corresponding damping factors; ε_∞ is the dielectric constant, at high frequencies, due to the electronic polarization.

As predicted by group-theory, eight infrared phonons were taken into account to describe the complex dielectric tensor composed by the components $\varepsilon_{px}(\omega)$ and $\varepsilon_{pz}(\omega)$, being divided into $4E_u$ and $4A_u$ modes. The symmetry assignment of the infrared phonons, as well as the first approximation for transverse and longitudinal frequencies was provided by DFT calculations, enabling us to specify between A_u and E_u polarizations and their respective optical modes. Fig. 5 summarizes the experimental and calculated infrared reflectance (a) and absorbance (b) spectra of ilmenite $CdTiO_3$ as pressed powder pellets and dilute dispersion, respectively. The values of volume concentration f were 0.56 and 0.13 for the reflectance and absorbance samples, respectively. The percolation thresholds sets, f_p and f_m, for both spectra were fitted to $f_p = 0.56$, 0.27, and $f_m = 0.95$ and 0.99. The effective thickness was found to be 2.17 μm. As the real thickness was 0.2 mm, we can roughly say that the nominal filling fraction is around three orders of magnitude smaller than the fitted one, which agrees reasonably well to the nominal value. The

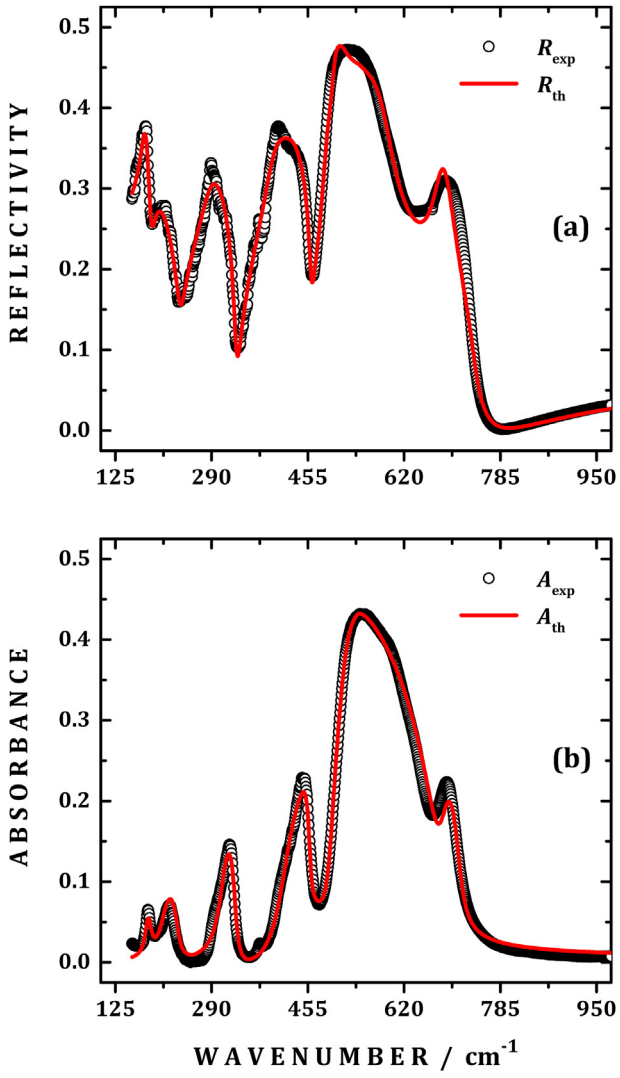

Fig. 5. Infrared reflectivity (a) and absorbance (b) spectra of ilmenite $CdTiO_3$ performed, at room conditions, in pressed powder pellets and dilute dispersion. Open circles denote the experimental data; red line represents the adjusted (calculated) via Eq (8)s and (9) in light of the average dielectric constant. (For interpretation of the references to colour in this figure legend, the reader is referred to the Web version of this article.)

effective concentration, defined as the thickness time the volume concentration, which basically represents the mass conservation principle, should be similar in the experimental system and as that of the fitting. More specifically, the experimental effective concentration is $(0.2\ \text{mm} \times 1 \times 10^{-3}) \sim 2 \times 10^{-4}$ mm, while fitting gives $(2.17 \times 10^{-3}\ \text{mm} \times 0.13) \sim 2.80 \times 10^{-4}$ mm, showing that, although particles tend to agglomerate, calculations give accurate values for IR absorption spectra. The quality of the adjustment process was assessed by the goodness of fit $\Re$ of 0.002.

6. Discussion

All the physical parameters fitted in accordance with the FPSQ models for polarization A_u and E_u in description of the complex dielectric tensor are listed in Table 1. It is also compared the transverse modes obtained in this work with those results reported by Baran and Boton [10,64], showing a reasonable agreement. In order to confirm the quality of the fitting procedure, the real part of $\langle\varepsilon\rangle$ and imaginary parts of $\langle\varepsilon\rangle$ and $1/\langle\varepsilon\rangle$ were directly extracted from the reflectivity spectrum by Kramers-Krönig (KK) analysis [65]. As shown in Fig. 6, there is a good agreement between KK data and those obtained by fitting with FPSQ method combined with EMT formula of Eq (2) in description of the effective dielectric constant. It should be highlighted that the imaginary parts of ε and $1/\varepsilon$ provide information on the frequencies and damping factors of the *TO* and *LO* optical branches, respectively.

The components $\varepsilon_{px}(\omega)$ and $\varepsilon_{pz}(\omega)$ of the complex dielectric tensor, experimentally derived for the Il-type $CdTiO_3$, appear in Fig. 7. The calculated positions of the transverse and longitudinal modes are listed in Table 1. One may note the good agreement between experimental and calculated data in view of the mode wavenumber. For each oscillator, or polar mode, adjusted by the FPSQ method, it is possible to define the dielectric strength $\Delta\varepsilon_j$ [66], as follows:

$$\Delta\varepsilon_j = \frac{\varepsilon_\infty}{\Omega_{jTO}^2} \cdot \frac{\prod_k \left(\Omega_{kLO}^2 - \Omega_{jTO}^2\right)}{\prod_{k\neq j} \left(\Omega_{kTO}^2 - \Omega_{jTO}^2\right)}. \tag{12}$$

This quantity allows us to estimate the *static* dielectric constant as a summation of all the strength values:

$$\varepsilon_s = \varepsilon_\infty + \sum_j \Delta\varepsilon_j, \tag{13}$$

which represents a limit condition of the complex dielectric function in Eq (11) for $\omega \ll \Omega_{jTO}$, close to the microwave regime. The value of ε_s can be also employed to calculate the dielectric loss associated with the individual polar mode:

$$\tan\delta_j = \omega \frac{\Delta\varepsilon_j \gamma_{jTO}}{\varepsilon_s \Omega_{jTO}^2}. \tag{14}$$

In particular, such estimation is useful to evaluate the possible applications of Il-type $CdTiO_3$ in microwave circuitry. The set of data is also summed up in Table 1.

The calculation results using DFT method are listed in Table 1 for comparison with those experimentally obtained. One may conclude that there is an excellent agreement between those results, in view of both transverse and longitudinal mode positions. Fig. 8 depicts the atomic displacement patterns for all the infrared modes in rhombohedral $CdTiO_3$, as derived from dynamic matrix solution. We will briefly discuss these modes in the next paragraphs.

Table 1
Dispersion parameters (Ω_{TO}, γ_{TO}, Ω_{LO}, γ_{LO}, in units of cm^{-1}) from the fit of the infrared reflectance spectrum of II-type $CdTiO_3$. The infrared phonon position (in units of cm^{-1}) calculated via DFT is also summarized.

Phonon N°	Experimental						DFT			Ref [10]
	Ω_{TO}	γ_{TO}	Ω_{LO}	γ_{LO}	$\Delta\varepsilon_j$	$10^6 \times \tan\delta_j/\omega$	Ω_{TO}	Ω_{LO}	$\Delta\varepsilon_j$	Ω_j
A_u (extraordinary)										
1	184.0	33.5	242.2	8.3	9.34	462.4	167	244	9.32	220
2	425.8	28.6	461.0	5.4	3.29	26.0	375	377	0.10	375
3	484.0	10.8	586.2	63.8	1.34	3.1	492	604	2.53	600
4	674.6	33.6	744.9	14.5	0.51	1.9	682	751	0.37	696
	ε_∞^z	5.5		$\sum\tan\delta_j/\omega$	4.933×10^{-4}		ε_∞^z	4.15		
	ε_s^z	19.98		$Q_u \times f$	60,769 GHz		ε_s^z	16.47		
E_u (ordinary)										
5	174.7	11.4	185.3	11.5	4.12	56.4	169	178	3.20	215
6	283.1	36.4	332.9	10.1	10.29	170.9	279	328	8.60	318
7	394.0	30.6	465.8	60.5	5.57	40.1	396	451	4.72	440
8	497.8	9.9	752.9	54.1	1.89	2.8	482	749	2.11	535
	ε_∞^x	5.5		$\sum\tan\delta_j/\omega$	2.701×10^{-4}		ε_∞^x	4.88		
	ε_s^x	27.37		$Q_u \times f$	110,979 GHz		ε_s^x	23.50		

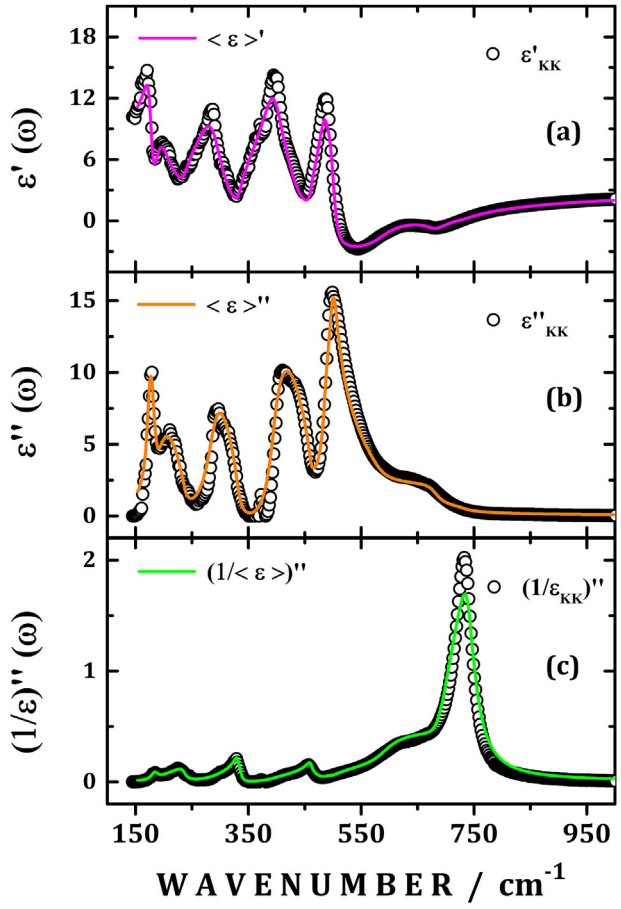

Fig. 6. Real (a) and imaginary (b) parts of the average dielectric constant ⟨ε⟩ of II-type $CdTiO_3$ in the infrared region. In part (c), the imaginary part of the reciprocal ⟨ε⟩ is also represented. Open circles denote the data extracted from the reflectivity spectrum by Kramers-Krönig analysis. Solid lines represent those data from the fitting procedure in light of the EMT formula of Eq (2).

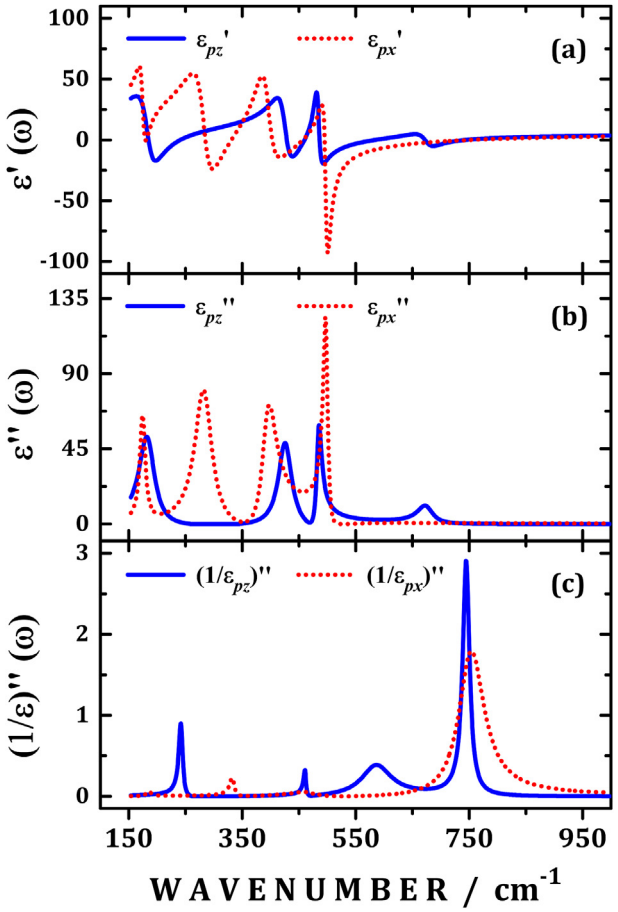

Fig. 7. Real (a) and imaginary (b) parts of the components $\varepsilon_{px}(\omega)$ and $\varepsilon_{pz}(\omega)$ of the complex dielectric tensor for ilmenite $CdTiO_3$. The imaginary parts of the reciprocal components are plotted in part (c).

For the A_u-like modes, the Cd and Ti atoms only move parallel to the C_3 main axis. The A_u mode at 184 cm^{-1} (DFT: 167 cm^{-1}) concerns the displacements of Cd and Ti along $[111]_R$ direction. Due to the effective charge motion along C_3 axis, the dipole moment generated contributes to ~47% for the *static* dielectric constant ε_s^z, in view of its dielectric strength $\Delta\varepsilon_1 = 9.34$. In a similar manner, the A_u mode at 426 cm^{-1} (DFT: 375 cm^{-1}) is described by the parallel movements of Cd ions against the oxygen sublattice, while oxygen anions move in-plane as asymmetric breathing. The effective charge motion produces a dipole moment with dielectric strength $\Delta\varepsilon_2 = 3.29$, and then contributing to ~17% for *static* dielectric constant along-*z*. The A_u mode located at 484 cm^{-1} (DFT: 492 cm^{-1}) has effective charge from oxygens and cation displacements which cancel each other out, and then producing a dielectric strength

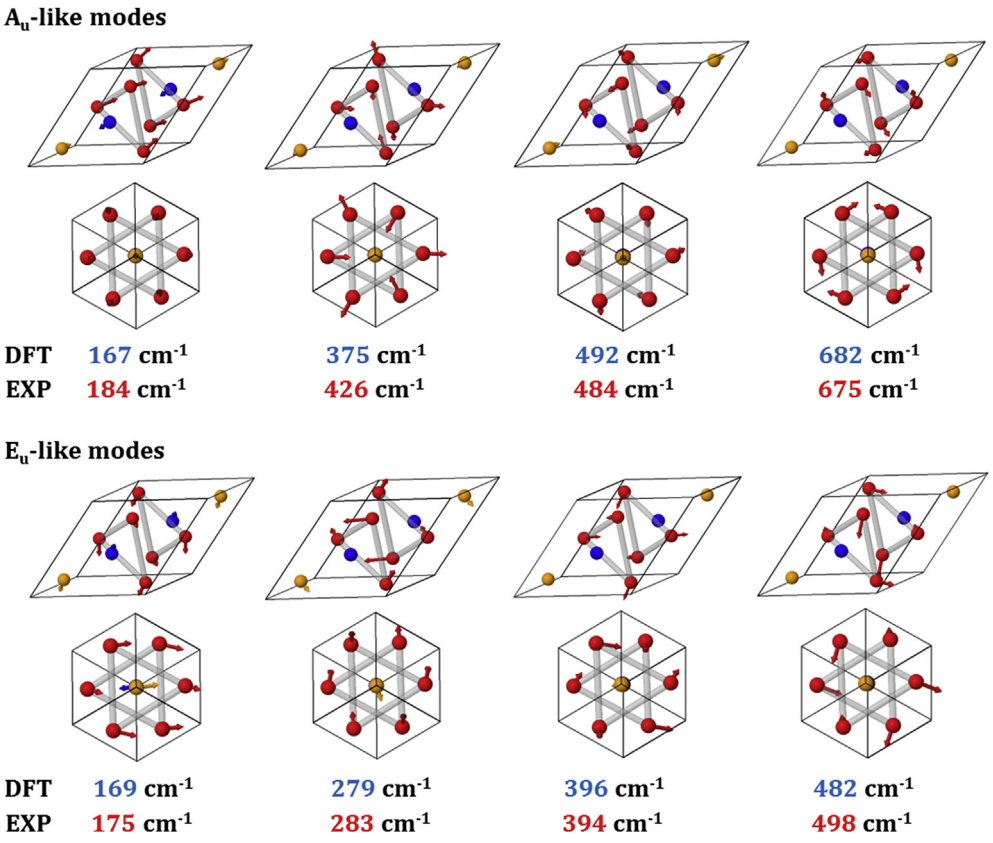

Fig. 8. Representation of the infrared modes ($4A_u \oplus 4E_u$) with calculated wavenumbers right below. The relative amplitude of the vibrations is also represented. There are two perspectives: tridimensional (top-row) one and along the $[111]_R$ projection (bottom-row). The orange, blue, and red spheres represent cadmium, titanium, and oxygen atoms, respectively. (For interpretation of the references to colour in this figure legend, the reader is referred to the Web version of this article.)

almost one ($\Delta\varepsilon_3 = 1.34$). Similar behavior was found for the A_u mode at 675 cm^{-1} (DFT: 682 cm^{-1}), which denotes the in-plane oxygen bending-type motions and then producing a low dielectric strength ($\Delta\varepsilon_4 = 0.51$).

For the E_u-like modes, the Cd and Ti atomic displacements lie at the orthogonal planes to the 3-fold axis (C_3). The low wavenumber E_u mode at 175 cm^{-1} (DFT: 169 cm^{-1}) has out-phase displacement of Cd and Ti atoms. The effective charge motion produces a dipolar moment with dielectric strength $\Delta\varepsilon_5 = 4.12$, as a consequence of cadmium and oxygen ions moving against titanium ones. The E_u mode located at 283 cm^{-1} (DFT: 279 cm^{-1}) has the strongest dielectric strength of $\Delta\varepsilon_6 = 10.29$. In this case, the effective charge motion is oriented along $[100]_h$ direction and contributing with 38% for the *static* dielectric constant ε_s^x. The E_u mode at 394 cm^{-1} (DFT: 396 cm^{-1}) also has an important participation (~20%) for dipolar moment with $\Delta\varepsilon_7 = 5.57$. Such a mode is described by Cd atoms displacements against oxygen sublattice in a bending-type motion. The E_u mode at 498 cm^{-1} (DFT: 482 cm^{-1}) has mainly torsional motions of oxygen anions that produce a low dipolar moment with 7% of contribution for the *static* dielectric constant: $\Delta\varepsilon_8 = 1.89$.

Different from the simple cubic $ATiO_3$ perovskite phase, which has three triply degenerate infrared modes ($\Gamma_{IR} = 3T_{1u}$) at Brillouin zone-center, the ilmenite phase has an enlarged number of infrared modes as a consequence of its high distortion. The change in site symmetry is expected, since $CdTiO_3$ ($t \sim 0.924$) [67] has a lower tolerance factor when compared with cubic perovskite, such as $SrTiO_3$ ($t \sim 1$). In the distortional process, a symmetry lowering at the A and Ti sites takes place from O_h to C_3, leading to the degeneracy breaking of T_{1u} mode into $A_u \oplus E_u$. In this way, the infrared modes in ilmenites can be correlated to those in perovskites. As summarized in Hlinka et al. [68], the infrared phonon spectrum in cubic perovskites is better understood by using three different eigenvectors of the Last, Slater, and Axe zone-center modes. Last mode has low wavenumber, being it ascribed to displacements of A cations against rigid TiO_6 octahedra. Slater one produces highest dipole moment due to its ferroelectric character, and then effectively contributing for the *static* dielectric constant. Axe mode resembles more closely the bending of octahedra and then with highest wavenumber.

In this sense, the infrared phonon spectrum in *R*-3 ilmenite structure depicts some similarities and differences in comparison to that in cubic perovskite. For instance, Last-type mode in ilmenite can be those at 175 (E_u, #5) and 184 (A_u, #1) cm^{-1} due to the Cd^{2+} role during the lattice vibration. Slater-type modes are located at 290–490 cm^{-1} region (modes #2, #3, #6, and #7), in which positive and negative charges move against each other. The highest wavenumber mode #4 (~675 cm^{-1}) can be seen as Axe-type because it has almost negligible contribution to the *static* dielectric constant ε_s^z. Nevertheless, the E_u mode at 498 cm^{-1} (#8) can be also defined as Axe-type, despite its high dipole moment. Such a fact is ascribed to an unusual combination of bending and asymmetric stretching motions of oxygen anions. Although the A_u mode at 184 cm^{-1} was classified as Last-type, its contribution to the *static* dielectric constant is higher than that from any other Slater-type mode.

Based on the optical constants listed in Table 1, a possible application of Il-type $CdTiO_3$ as a central element in microwave device engineering can be postulated. A material that fulfills the design details should possess a high unloaded quality factor $Q_u = 1/\tan\delta$, in order to provide selectivity to the circuitry; relatively high

dielectric constant in microwave region for miniaturization improvements, and temperature coefficient of resonant frequency very close to zero which leads to device thermal stability [69]. For the ilmenite $CdTiO_3$, the values of *static* dielectric constant $\varepsilon_s^x = 27.37$ and $\varepsilon_s^z = 19.98$ denote extrapolations of the dielectric tensor for $\omega \rightarrow 0$, and then for the IEEE X-band centered around 10 GHz (f ~0.334 cm^{-1}). Although the dielectric constant found in Il-type $CdTiO_3$ are not so high for applications in X-band circuitry, the values for the dielectric losses seem to be very promising. Such a factor depends on the contribution of the individual polar mode, as follows: $\tan\delta = \sum \tan\delta_j$. The values listed in Table 1 lead to the 10 GHz dielectric loss near 1.6×10^{-4} and 9.0×10^{-5} both A_u and E_u polarizations, respectively. It means that unloaded quality factors $Q_u \times f$ for ordinary modes have interesting magnitudes close to 110,979 GHz. Since Il-type $CdTiO_3$ is structurally unstable in large particle size, new strategies based doping with isovalent and isomorphic ions at A-site are welcome in developing dense ceramics for final microwave uses.

7. Conclusion

In summary, we presented a detailed analysis of the infrared active phonon spectrum of ilmenite $CdTiO_3$ using infrared specular reflectance and absorption spectroscopy. A combination of experimental and theoretical methods was applied to investigate the polar modes in rhombohedral R-3 (C_{3i}^2) ilmenite phase. The phonon frequencies of this phase makes specially difficult to employ previously published methods for the determination of the effective dielectric constant, so that we modified a previous model to accurately determine the spectral features of small modes close to the longitudinal frequencies of strong ones, and we have also implemented a fitting procedure which combines information from reflectance and absorption to eliminate possible ambiguities for modes with close transverse frequencies at different polarizations. Intrinsic dielectric response was extrapolated to the microwave region, showing that the values of the components of static dielectric constants are ε_s^x ~27 and ε_s^z ~20. Very promising values for the unloaded quality factor were found for Il-type $CdTiO_3$, $Q_u \times f$ ~111,000 GHz, enabling possible application for circuitry at IEEE X-band of 10 GHz.

Acknowledgements

Brazilian agencies CAPES (Proc. Number: 88881.171031/2018-01), FAPESP (Proc. Numbers: 2013/07793-6, 2019/08928-9, and 2013/07296-2), and CNPq (Proc. Number: 432242/2018-0) are acknowledged due to the financial support. José A. Alonso thanks the Spanish Ministry of Science, Innovation, and Universities for funding the project MAT2017-84496-R. Y. Huttel acknowledges the Spanish Ministry of Science, Innovation, and Universities for funding through project MAT2014-59772-C2-2-P. J.E. Rodrigues thanks Antonio C. Hernandes for scanning electron microscopy measurements and Carlos Pecharromán to the Service of IR spectroscopy and ellipsometry of the "Instituto de Ciencia de Materiales de Madrid-CSIC".

References

[1] P. Dhivya, A.K. Prasad, M. Sridharan, Nanostructured perovskite $CdTiO_3$ films for methane sensing, Sens. Actuators B Chem. 222 (2016) 987–993.
[2] Z. Imran, S.S. Batool, H. Jamil, M. Usman, M. Israr-Qadir, S.H. Shah, et al., Excellent humidity sensing properties of cadmium titanate nanofibers, Ceram. Int. 39 (2013) 457–462.
[3] F.A. Hernández-García, G. Torres-Delgado, R. Castanedo-Pérez, O. Zelaya-Ángel, Photodegradation of gaseous C_6H_6 using CdO+$CdTiO_3$ and TiO_2 thin films obtained by sol–gel technique, J. Photochem. Photobiol. A Chem. 310 (2015) 52–59.
[4] M.A. Ehsan, H. Khaledi, A. Pandikumar, N.M. Huang, Z. Arifin, M. Mazhar, Dye sensitized solar cell applications of $CdTiO_3$–TiO_2 composite thin films deposited from single molecular complex, J. Solid State Chem. 230 (2015) 155–162.
[5] H. Moriwake, A. Kuwabara, C.A.J. Fisher, H. Taniguchi, M. Itoh, I. Tanaka, First-principles calculations of lattice dynamics in $CdTiO_3$ and $CaTiO_3$: phase stability and ferroelectricity, Phys. Rev. B. 84 (2011) 104114.
[6] B.J. Kennedy, Q. Zhou, S. Zhao, F. Jia, W. Ren, K.S. Knight, Low-temperature structure and the ferroelectric phase transitions in the $CdTiO_3$ perovskite, Phys. Rev. B. 96 (2017) 214105.
[7] B.J. Kennedy, Q. Zhou, M. Avdeev, The ferroelectric phase of $CdTiO_3$: a powder neutron diffraction study, J. Solid State Chem. 184 (2011) 2987–2993.
[8] H. Taniguchi, H.P. Soon, T. Shimizu, H. Moriwake, Y.J. Shan, M. Itoh, Mechanism for suppression of ferroelectricity in $Cd_{1-x}Ca_xTiO_3$, Phys. Rev. B Condens. Matter Mater. Phys. 84 (2011) 1–5.
[9] R.C. Liebermann, Elasticity of the ilmenite - perovskite phase transformation in $CdTiO_3$, Earth Planet. Sci. Lett. 29 (1976) 326–332.
[10] E.J. Baran, I.L. Botto, Die IR-Spektren einiger Doppeloxide mit Ilmenit-Struktur, Z. Anorg. Allg. Chem. 444 (1978) 282–288.
[11] A.M. Hofmeister, IR reflectance spectra of natural ilmenite: comparison with isostructural compounds and calculation of thermodynamic properties, Eur. J. Mineral. 5 (1993) 281–296.
[12] V.L. Gurevich, A.K. Tagantsev, Intrinsic dielectric loss in crystals, Adv. Phys. 40 (1991) 719–767.
[13] F. Gervais, B. Piriou, Temperature dependence of transverse- and longitudinal-optic modes in TiO_2 (rutile), Phys. Rev. B. 10 (1974) 1642–1654.
[14] K. Wakino, M. Murata, H. Tamura, Far infrared reflection spectra of Ba(Zn,Ta)O_3-$BaZrO_3$ dielectric resonator material, J. Am. Ceram. Soc. 69 (1986) 34–37.
[15] H. Tamura, D.A. Sagala, K. Wakino, Lattice vibrations of $Ba(Zn_{1/3}Ta_{2/3})O_3$ crystal with ordered perovskite structure, Jpn. J. Appl. Phys. 25 (1986) 787–791.
[16] C. Pecharroman, J.E. Iglesias, A method for the determination of infrared optical constants from reflectance measurements on powdered samples, J. Phys. Condens. Matter 6 (1994) 7125–7141.
[17] C. Pecharromán, J.E. Iglesias, Effective dielectric properties of packed mixtures of insulator particles, Phys. Rev. B. 49 (1994) 7137–7147.
[18] C. Pecharromán, T. González-Carreño, J. Iglesias, The infrared dielectric properties of maghemite, γ-Fe_2O_3, from reflectance measurement on pressed powders, Phys. Chem. Miner. 22 (1995) 21–29.
[19] C. Pecharromán, T. González-Carreño, J.E. Iglesias, The infrared dielectric properties of η–Al_2O_3, J. Mater. Res. 11 (1996) 127–133.
[20] C. Pecharromán, J.M. Amarilla, Thermal evolution of infrared vibrational properties of $Li_{4/3}Ti_{5/3}O_4$ measured by specular reflectance, Phys. Rev. B. 62 (2000) 12062–12068.
[21] C. Pecharromán, M. Ocaña, C.J. Sema, Optical constants of tetragonal and cubic zirconias in the infrared, J. Appl. Phys. 80 (1996) 3479–3483.
[22] C. Pecharromán, J.E. Iglesias, Effect of particle shape on the IR reflectance spectra of pressed powders of anisotropic materials, Appl. Spectrosc. 54 (2000) 634–638.
[23] S. Onari, T. Arai, K. Kudo, Infrared lattice vibrations and dielectric dispersion in α–Fe_2O_3, Phys. Rev. B. 16 (1977) 1717–1721.
[24] C.J. Winta, M. Wolf, A. Paarmann, Low-temperature infrared dielectric function of hyperbolic α-quartz, Phys. Rev. B. 99 (2019) 144308.
[25] A. Bartasyte, S. Margueron, A.M. Glazer, E. Simon, I. Gregora, S. Huband, et al., Vibrational modes and overlap matrix of $LiNb_{1-x}Ta_xO_3$, Phys. Rev. B. 99 (2019) 94306.
[26] A. Mock, R. Korlacki, S. Knight, M. Stokey, A. Fritz, V. Darakchieva, et al., Lattice dynamics of orthorhombic $NdGaO_3$, Phys. Rev. B. 99 (2019) 184302.
[27] J.E. Rodrigues, M.M. Ferrer, T.R. Cunha, R.C. Costa, J.R. Sambrano, A.D. Rodrigues, et al., First-principles calculations and Raman scattering evidence for local symmetry lowering in rhombohedral ilmenite: temperature- and pressure-dependent studies, J. Phys. Condens. Matter 30 (2018) 485401.
[28] J. Rodríguez-Carvajal, Recent advances in magnetic structure determination by neutron powder diffraction, Phys. B Phys. Condens. Matter. 192 (1993) 55–69.
[29] R. Nevshupa, L. Martínez, L. Álvarez, M.F. López, Y. Huttel, J. Méndez, et al., Influence of thermal ageing on surface degradation of ethylene-propylene-diene elastomer, J. Appl. Polym. Sci. 119 (2011) 242–251.
[30] A.D. Becke, Density-functional thermochemistry. III. The role of exact exchange, J. Chem. Phys. 98 (1993) 5648–5652.
[31] C. Lee, W. Yang, R.G. Parr, Development of the Colle-Salvetti correlation-energy formula into a functional of the electron density, Phys. Rev. B. 37 (1988) 785–789.
[32] J. Laun, D. Vilela Oliveira, T. Bredow, Consistent Gaussian basis sets of double- and triple-zeta valence with polarization quality of the fifth period for solid-state calculations, J. Comput. Chem. 39 (2018) 1285–1290.
[33] G. Sophia, P. Baranek, C. Sarrazin, M. Rérat, R. Dovesi, First-principles study of the mechanisms of the pressure-induced dielectric anomalies in ferroelectric perovskites, Phase Transitions 86 (2013) 1069–1084.
[34] L. Maschio, B. Kirtman, R. Orlando, M. Rèrat, *Ab initio* analytical infrared intensities for periodic systems through a coupled perturbed Hartree-Fock/Kohn-Sham method, J. Chem. Phys. 137 (2012) 204113.
[35] L. Maschio, B. Kirtman, M. Rérat, R. Orlando, R. Dovesi, *Ab initio* analytical Raman intensities for periodic systems through a coupled perturbed Hartree-Fock/Kohn-Sham method in an atomic orbital basis. II. Validation and

comparison with experiments, J. Chem. Phys. 139 (2013) 164102.
[36] T.R. Cunha, A.D. Rodrigues, J.E. Rodrigues, R.C. da Costa, T.A. Toledo, P.S. Pizani, Combining XRD and Raman spectroscopy techniques to probe the solid solution and composite forms of $Pb_{1-x}Co_xTiO_3$ systems, Mater. Res. Bull. 107 (2018) 462–467.
[37] A. Deshpande, P. Shah, R.S. Gholap, N.M. Gupta, Interfacial and physicochemical properties of polymer-supported CdS-ZnS nanocomposites and their role in the visible-light mediated photocatalytic splitting of water, J. Colloid Interface Sci. 333 (2009) 263–268.
[38] L. Wu, J.C. Yu, X. Fu, Characterization and photocatalytic mechanism of nanosized CdS coupled TiO_2 nanocrystals under visible light irradiation, J. Mol. Catal. A Chem. 244 (2006) 25–32.
[39] P. Roy, S.K. Srivastava, A new approach towards the growth of cadmium sulphide thin film by CBD method and its characterization, Mater. Chem. Phys. 95 (2006) 235–241.
[40] B. Erdem, R.A. Hunsicker, G.W. Simmons, E.D. Sudol, V.L. Dimonie, M.S. El-Aasser, XPS and FTIR surface characterization of TiO_2 particles used in polymer encapsulation, Langmuir 17 (2001) 2664–2669.
[41] U. Diebold, T.E. Madey, TiO_2 by XPS, Surf. Sci. Spectra 4 (1996) 227–231.
[42] T.-C. Wei, Y.-H. Chang, P. Zhai, P.C.H. Cheung, Y.-T. Huang, S.-P. Feng, et al., The synthesis of Nb-doped TiO_2 nanoparticles for improved-performance dye sensitized solar cells, Electrochim. Acta 182 (2015) 230–237.
[43] L.F. da Silva, W. Avansi, A.C. Catto, J.E.F.S. Rodrigues, M.I.B. Bernardi, V.R. Mastelaro, The role of Nb addition in TiO_2 nanoparticles: phase transition and photocatalytic properties, Phys. Status Solidi 215 (2018) 1800321.
[44] S. Major, S. Kumar, M. Bhatnagar, K.L. Chopra, Effect of hydrogen plasma treatment on transparent conducting oxides, Appl. Phys. Lett. 49 (1986) 394–396.
[45] M. Chen, X. Wang, Y.H. Yu, Z.L. Pei, X.D. Bai, C. Sun, et al., X-ray photoelectron spectroscopy and auger electron spectroscopy studies of Al-doped ZnO films, Appl. Surf. Sci. 158 (2000) 134–140.
[46] D.L. Rousseau, R.P. Bauman, S.P.S. Porto, Normal mode determination in crystals, J. Raman Spectrosc. 10 (1981) 253–290.
[47] T.G. Mayerhöfer, Modelling IR spectra of single-phase polycrystalline materials with random orientation in the large crystallites limit-extension to arbitrary crystal symmetry, J. Opt. A Pure Appl. Opt. 4 (2002) 540–548.
[48] S. Kirkpatrick, Percolation and conduction, Rev. Mod. Phys. 45 (1973) 574–588.
[49] D.J. Bergman, The dielectric constant of a composite material—a problem in classical physics, Phys. Rep. 43 (1978) 377–407.
[50] D.A.G. Bruggeman, Berechnung verschiedener physikalischer Konstanten von heterogenen Substanzen. I. Dielektrizitätskonstanten und Leitfähigkeiten der Mischkörper aus isotropen substanzen, Ann. Phys. 416 (1935) 636–664.
[51] C. Pecharromàn, J.E. Iglesias, Modeling particle size and clumping effects in the IR absorbance spectra of dilute powders, Appl. Spectrosc. 50 (1996) 1553–1562.
[52] C. Pecharromán, J.S. Moya, Experimental evidence of a giant capacitance in insulator-conductor composites at the percolation threshold, Adv. Mater. 12 (2000) 294–297.
[53] C. Pecharromán, F. Esteban-Betegón, J.F. Bartolomé, S. López-Esteban, J.S. Moya, New percolative $BaTiO_3$–Ni composites with a high and frequency-independent dielectric constant ($\varepsilon_r \approx 80000$), Adv. Mater. 13 (2001) 1541.
[54] C. Pecharromán, S. López-Esteban, J.F. Bartolomé, J.S. Moya, Evidence of nearest-neighbor ordering in wet-processed zirconia-nickel composites, J. Am. Ceram. Soc. 84 (2004) 2439–2441.
[55] C. Pecharromán, J.F. Bartolomé, J. Requena, J.S. Moya, S. Deville, J. Chevalier, et al., Percolative mechanism of aging in zirconia-containing ceramics for medical applications, Adv. Mater. 15 (2003) 507–511.
[56] L. Fernandez-Garcia, M. Suárez, J.L. Menéndez, C. Pecharromán, D. Nuzhnyy, V. Bovtun, et al., Dielectric properties of carbon nanofibre/alumina composites, Carbon N. Y. 57 (2013) 380–387.
[57] L. Fernández-García, M. Suárez, J.L. Menéndez, C. Pecharromán, R. Menéndez, R. Santamaría, Dielectric behavior of ceramic–graphene composites around the percolation threshold, Nanoscale Res. Lett. 10 (2015) 1–7.
[58] C. Pecharromán, J.E. Iglesias, Effect of particle shape on the IR reflectance spectra of pressed powders of anisotropic materials, Appl. Spectrosc. 54 (2000) 634–638.
[59] C. Pecharromán, F. Gracía, J.P. Holgado, M. Ocaña, A.R. González-Elipe, J. Bassas, et al., Determination of texture by infrared spectroscopy in titanium oxide-anatase thin films, J. Appl. Phys. 93 (2003) 4634–4645.
[60] C. Pecharromán, I. Sobrados, J.E. Iglesias, T. González-Carreño, J. Sanz, Thermal evolution of transitional aluminas followed by NMR and IR spectroscopies, J. Phys. Chem. B 103 (1999) 6160–6170.
[61] C. Pecharromán, F.J. Gordillo-Vázquez, Expansion of the spectral representation function of a composite material in a basis of Legendre polynomials: experimental determination and analytic approximations, Phys. Rev. B. 74 (2006) 35120.
[62] J.R. Jasperse, A. Kahan, J.N. Plendl, S.S. Mitra, Temperature dependence of infrared dispersion in ionic crystals LiF and MgO, Phys. Rev. 146 (1966) 526–542.
[63] L. Genzel, T.P. Martin, Infrared absorption in small ionic crystals, Phys. Status Solidi 51 (1972) 91–99.
[64] E.J. Baran, I.L. Botto, Die Raman-Spektren von $ZnTiO_3$ und $CdTiO_3$, Z. Anorg. Allg. Chem. 448 (1979) 188–192.
[65] W. Hayes, R. Loudon, Scattering of Light by Crystals, Dover, New York, 2004.
[66] J. Hlinka, T. Ostapchuk, D. Noujni, S. Kamba, J. Petzelt, Anisotropic dielectric function in polar nanoregions of relaxor ferroelectrics, Phys. Rev. Lett. 96 (2006) 27601.
[67] S.G. Kang, First-principles examination of low tolerance factor perovskites, Int. J. Quantum Chem. 117 (2017) 1–9.
[68] J. Hlinka, J. Petzelt, S. Kamba, D. Noujni, T. Ostapchuk, Infrared dielectric response of relaxor ferroelectrics, Phase Transitions 79 (2006) 41–78.
[69] M. Sebastian, Dielectric Materials for Wireless Communication, first ed., Elsevier, 2008.